PAPER

Highly efficient and ultra-stable CsPbBr₃ composites for LCD devices and X-ray imaging†

Peng Wang,‡[abc] Zhaoyu Wang,‡[d] Meiyi Zhu,‡[abc] QiuTing Cai,[abc] Hanyan Huang,[abc] Chengyuan Tang,[abc] Haoran Zhang,[abc] Chao Fan, [ID] *[abce] Xingliang Dai, [ID] [abce] Haiping He [ID] *[abce] and Zhizhen Ye*[abce]

Achieving excellent optical properties and stability is crucial for the practical utilization of perovskite emitters. Herein, ultra-stable CsPbBr₃-DPSI/MS composites with a high photoluminescence quantum yield (PLQY) of 93.2% are obtained through passivation of the surface of CsPbBr₃ quantum dots (QDs) by 3-(decyldimethylammonio)-propane-sulfonate inner salt (DPSI) and encapsulating these QDs using silica molecular sieve (MS) templates. After aging for 1000 hours under harsh synergistic conditions (*i.e.*, temperature of 60 °C, relative humidity of 90%, and blue light irradiation with a power density of 3500 W m⁻²), these composites still retain 90% of their initial photoluminescence (PL) intensity. To the best of our knowledge, these CsPbBr₃-DPSI/MS composites represent the most stable CsPbBr₃ emitters in an accelerated aging test under these synergistic humidity–heat–light conditions. The liquid crystal display (LCD) backlight module utilizing these stable composites shows a wide color gamut of 111.7% NTSC. Furthermore, these CsPbBr₃-DPSI/MS composites exhibit exceptional X-ray scintillator performance and impressive radiation hardness, delivering a high X-ray imaging spatial resolution of up to ≈16 lp mm⁻¹ and a low detection limit of 339 nGy$_{air}$ s⁻¹.

1. Introduction

All-inorganic CsPbX₃ (X = Cl, Br, I) quantum dots (QDs) possess excellent optical and electrical properties,[1] including a widely tunable bandgap,[2] narrow emission width,[3] and high photoluminescence quantum yield (PLQY).[4] These properties make them promising candidates for various optoelectronic applications such as full-color liquid crystal displays (LCD),[5,6] light-emitting diodes (LED),[7,8] solar cells,[9,10] and X-ray detectors.[11,12] Despite these merits, the severe structural instability deriving from their vulnerable ionic bond remains a major obstacle to

[a] *School of Materials Science and Engineering, State Key Laboratory of Silicon and Advanced Semiconductor Materials, Zhejiang University, Hangzhou 310027, P. R. China. E-mail: chaofan@hnu.edu.cn, hphe@zju.edu.cn, yezz@zju.edu.cn*

[b] *Wenzhou Key Laboratory of Novel Optoelectronic and Nano Materials, Zhejiang Provincial Engineering Research Center of Oxide Semiconductors for Environmental and Optoelectronic Applications, Institute of Wenzhou, Zhejiang University, Wenzhou 325006, P. R. China*

[c] *Wenzhou XINXINTAIJING Tech. Co. Ltd, Wenzhou, 325006, P. R. China*

[d] *State Key Laboratory of Structural Chemistry, Fujian Institute of Research on the Structure of Matter, Chinese Academy of Sciences Fuzhou, Fujian 350002, P. R. China*

[e] *Shanxi-Zheda Institute of Advanced Materials and Chemical Engineering, Shanxi, 030000, P. R. China*

† Electronic supplementary information (ESI) available. See DOI: https://doi.org/10.1039/d3tc04701f

‡ These authors contributed equally to this work.

their industrialization.[13–15] Exposure to moisture, oxygen, high-energy light, or heat can cause CsPbX₃ QDs to undergo a phase transition or generate surface defects, resulting in an irreversible luminescence quenching.[16] Fortunately, the stability of CsPbX₃ QDs can be improved *via* shelling to reduce surface defects and insulate these QDs from the external environment.[17] For instance, Bakr *et al.* demonstrated that zwitterionic lecithin ligands can stabilize the perovskite phase of CsPbI₃ QDs for long periods in air.[18] Kovalenko *et al.* reported that the surface passivation in CsPbBr₃/KBr nanocomposites suppresses the PL thermal quenching of CsPbBr₃ QDs.[19] Although many efforts have been made to boost either the moisture-, thermal-, or photostability of CsPbX₃ QDs, the developed CsPbX₃ QDs still cannot tolerate the real application atmosphere of synergistic humidity, heat, and high-energy light irradiation.[20]

One of the promising strategies to improve the overall (thermal-, moisture-, and photo-) stability of CsPbX₃ QDs is to encapsulate them in robust inorganic matrices, such as metal oxides (*e.g.*, SiO₂ and Al₂O₃),[21–25] or glasses.[26–30] These matrices isolate CsPbX₃ QDs from moisture and O₂, prevent ion migration, and inhibit inter-particle fusion at high temperature.[22] Studies have demonstrated that CsPbX₃ QDs embedded in inorganic matrix templates can survive in water, acidic solution, and heating for a long time.[31] However, these inorganic matrices tend to be amorphous or possess a mismatched lattice constant with CsPbX₃, which results in a lack of surface

This journal is © The Royal Society of Chemistry 2024

J. Mater. Chem. C, 2024, **12**, 3465–3473 | **3465**

passivation effect for inside $CsPbX_3$ QDs. Consequently, the enrichment of surface defects adversely impacts PLQY and photo-stability.[32–34] For example, Xuan *et al.* reported $CsPbBr_3$: Sr/PbBr(OH)/silicon oxide composites with high stability when exposed to water and heat. However, these composites showed unsatisfactory photo-stability, with only 54% of their initial PL intensity being retained after aging for 720 minutes under blue light with an intensity of 1500 W m^{-2}.[35] Zhang *et al.* reported that $CsPbBr_3$ QDs embedded in silica can survive in water for 50 days without a visible drop in PL intensity, but exhibit a relatively low PLQY of 63%.[22]

Herein, we show $CsPbBr_3$ QDs with both highly efficient and overall stability, which is achieved by *in situ* passivation and encapsulation of $CsPbBr_3$ QDs in silica molecular sieve (MS) templates through a solid-state synthesis. Briefly, the obtained $CsPbBr_3$ QDs are passivated by 3-(decyldimethylammonio)-propane-sulfonate inner salt (DPSI) and encapsulated by silica MS matrices. The resulting $CsPbBr_3$-DPSI/MS composites exhibit a high PLQY of 93.2% and significantly improved stability against water, heat, and blue light irradiation. Even after aging for 1000 hours under harsh synergistic conditions (*i.e.*, temperature of 60 °C, relative humidity of 90%, and blue light irradiation with a power density of 3500 W m^{-2}), these $CsPbBr_3$-DPSI/MS composites still retain 90% of their initial PL intensity. An LCD device presenting a wide color gamut of 111.7% National Television Standards Committee (NTSC) is obtained, when employing these stable composites as the green light source of the LCD backlight. Furthermore, the $CsPbBr_3$-DPSI/MS composites exhibit a promising foreground in high-performance X-ray imaging detectors, achieving a high spatial resolution of 16 lp mm^{-1} and a detection limit of 339 nGy$_{air}$ s^{-1} that is much lower than the requirement of X-ray medical diagnostics of ≈ 5.5 μGy$_{air}$ s^{-1}.

2. Experiment section

2.1 Materials

Cesium bromide (CsBr, 99.9%), lead bromide (PbBr$_2$, 99.9%), and 3-(decyldimethylammonio)-propane-sulfonate inner salt (DPSI, 98%) were purchased from Macklin. The MCM-41 MSs were purchased from XFNANO. Cyclohexane was purchased from Sinopharm Chemical Reagent Co., China. All the chemicals were used as-received without further purification.

2.2 Solid-state syntheses of CsPbBr$_3$-DPSI/MS composites

0.0425 g CsBr, 0.0733 g PbBr$_2$, and 0.0307 g DPSI were dispersed in 0.1505 g MCM-41 MS powder and the mixture was stirred for 20 min. The obtained powder was calcined at 560 °C for 30 min with a heating rate of 20 °C min^{-1} in a tube furnace with 1 in diameter quartz tube under an air atmosphere of 0.05 MPa. After cooling to room temperature at a cooling rate of 4.7 °C min^{-1}, the $CsPbBr_3$-DPSI/MS composites were acquired.

2.3 Preparation of scintillator films

The $CsPbBr_3$-DPSI/MS composite solution (≈ 0.1 g mL^{-1} in cyclohexane) was spin-coated on a glass substrate at 500 rpm for 30 s and then dried on the hot plate at 60 °C for 5 min. These procedures were repeated 5 times until the desired film thickness was achieved.

2.4 Fabrication of diffusion plates

Polystyrene plastic particles were mixed with $CsPbBr_3$-DPSI/MS composites in a twin-screw extruder with the 180 °C heating temperature. After the melt extrusion process, the $CsPbBr_3$-DPSI/MS composites were embedded in plastic. A plate molding press machine was used to turn these mixed particles into a diffusion plate.

2.5 Composition and structural characterization

Fourier-transform infrared spectroscopy data were measured using a Thermo Scientific Nicolet iS5 system. X-ray photoelectron spectroscopy data were measured using a Thermo Fisher, ESCALAB Xi+. Crystal structures were obtained using a Rigaku D/MAX 2500 with Cu-Kα sources ($\lambda = 0.1542$ nm) and a transmission electron microscope (TEM) (FEI Tecnai G2 F20). Elemental compositions of the samples were characterized *via* a TEM (FEI Tecnai G2 F20) combined with EDS.

2.6 Optical characterization

Steady-state and time-resolved PL spectra were measured using a Zolix Instruments OmniFluo900 spectrometer equipped with a picosecond pulsed laser diode (405 nm, 58.6 ps). Time- and wavelength-dependent PL mapping was performed with a streak camera (Zolix, ST10) under the illumination of a light conversion Pharos Yb:KGW laser (PHAROS PH2, 405 nm, 200 fs, 1 kHz). Spectral thermal stability was examined using a 405 nm continuous wave laser as the excitation source and an FX 2000 spectrometer to obtain the PL signals. Spectral photostability was examined using a 455 nm LED as the excitation source and an FX 2000 spectrometer to obtain the PL signals. PLQYs were evaluated by using a fluorescence spectrometer (Ocean Insight, QEPro) with an integrated sphere excited at a wavelength of 410 nm using an LED chip source.

2.7 Radioluminescence and X-ray imaging

Radioluminescence (RL) emission spectra and RL stability tests were performed using an X-ray source (Magpro, TUB00146-W06, 12 W) and a spectrometer (Edinburgh, FLS 980). X-ray images of samples were taken using the above-mentioned X-ray source and a QHY9701 camera without any filter. The radiation stability was tested under ambient air conditions with relative humidity of about 40–60% and temperature of about 15–25 °C.

3. Results and discussion

$CsPbBr_3$-DPSI/MS composites were synthesized through a solid-state synthesis method (Fig. 1), in which CsBr, PbBr$_2$, and DPSI powders were mixed with silica MS templates, and heated at
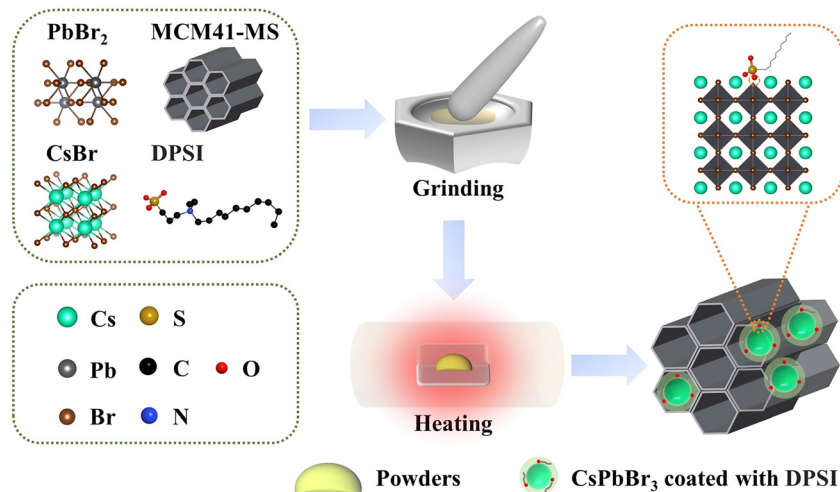
3466 | *J. Mater. Chem. C*, 2024, **12**, 3465–3473

This journal is © The Royal Society of Chemistry 2024

Fig. 1 Schematic of the syntheses of the $CsPbBr_3$-DPSI/MS composites and the defect passivation mechanism of DPSI.

560 °C for 30 min. During the heating process, CsBr reacted with $PbBr_2$ to form $CsPbBr_3$ QDs in the mesopores of silica MS templates, and DPSI tightly bound to the surface of the $CsPbBr_3$ QDs due to the interaction between the negatively charged SO_3^- group in DPSI and the uncoordinated Pb^{2+} in $CsPbBr_3$ QDs.[36]

With the heating going on, the porous structure of the silica MS templates gradually collapsed, encapsulating the internal QDs and ultimately obtaining the $CsPbBr_3$-DPSI/MS composites. Brunauer–Emmett–Teller (BET) and transmission electron microscopy (TEM) measurements were conducted to
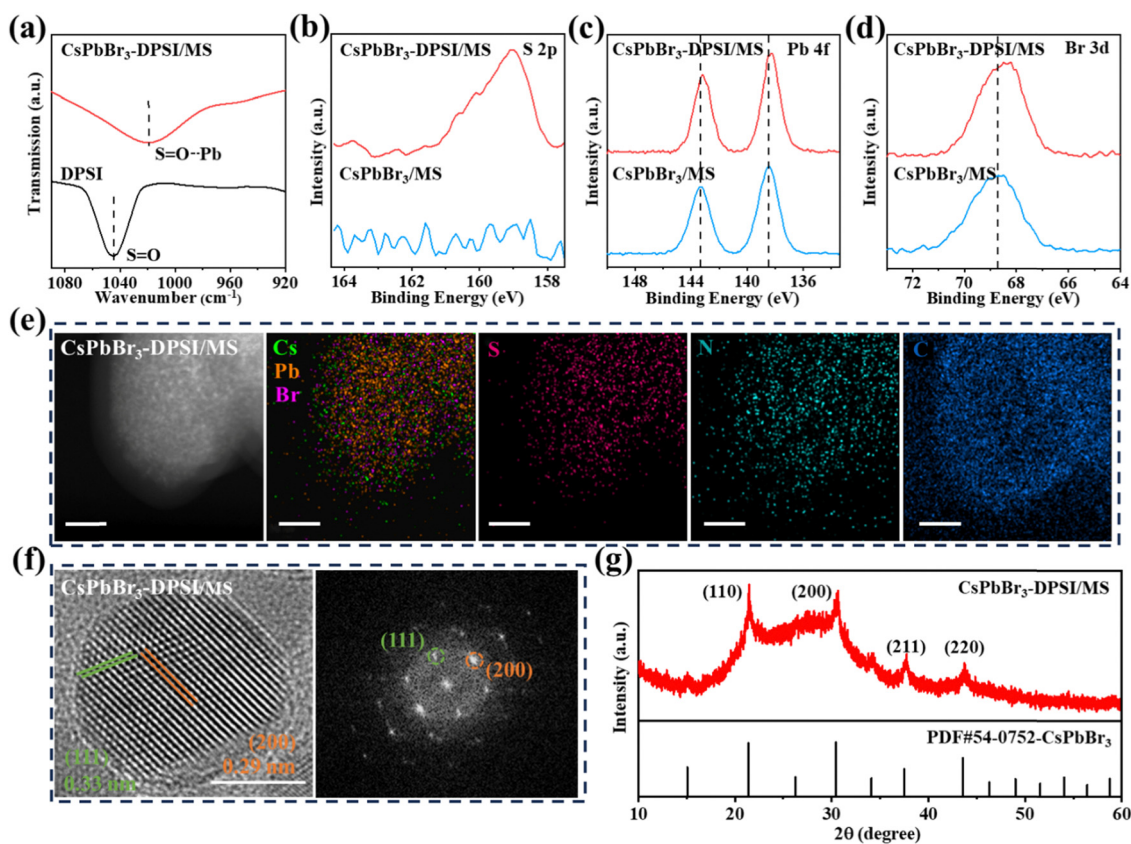

Fig. 2 Evidence of DPSI coordinating on the surface of $CsPbBr_3$ QDs and structural characterization of the $CsPbBr_3$ QDs. (a) FT-IR spectra of the DPSI and $CsPbBr_3$-DPSI/MS. XPS spectra for $CsPbBr_3$/MS and $CsPbBr_3$-DPSI/MS: (b) S 2p, (c) Pb 4f, (d) Br 3d. (e) TEM image and the corresponding elemental mapping images of the $CsPbBr_3$-DPSI/MS. Scale bar: 50 nm. (f) HRTEM image and the corresponding diffraction pattern obtained by FFT. Scale bar: 5 nm. (g) PXRD pattern of the $CsPbBr_3$-DPSI/MS.

This journal is © The Royal Society of Chemistry 2024

J. Mater. Chem. C, 2024, **12**, 3465–3473 | **3467**

characterize the collapse of MS templates (Fig. S1, ESI†). The BET result shows that the surface area of MS templates decreases from 998 to 15 $m^2\ g^{-1}$ after the solid-state syntheses, indicating that the porous structure of the MS templates gradually collapses during the heating process. Besides, the TEM image of original MS templates shows a wide distribution of mesoporous in the MS. After the solid-state synthesis, it can be observed that $CsPbBr_3$ nanocrystals were encapsulated in the MS, and the mesoporous structures of MS were collapsed.

The coordination of DPSI on the surface of $CsPbBr_3$ QDs was investigated by Fourier-transform infrared (FT-IR) spectroscopy and X-ray photoelectron spectroscopy (XPS). As shown in Fig. 2a, the S=O stretching vibration peak of DPSI at 1044 cm^{-1} shifts to a lower wavenumber of 1021 cm^{-1} in $CsPbBr_3$-DPSI/MS composites, indicating the lone electron pair donation from O of DPSI to the Pb^{2+} empty orbitals of $CsPbBr_3$.[37] The presence of DPSI in the obtained samples was further confirmed by the observation of S 2p and N 1s peaks in the XPS spectra (Fig. 2b and Fig. S2, ESI†). Meanwhile, the Pb 4f and Br 3d peaks of $CsPbBr_3$-DPSI/MS composites shift towards lower binding energy compared to those of the reference sample (Fig. 2c and d), indicating chemical interactions between the SO_3^- group in DPSI and the Pb^{2+} in $CsPbBr_3$ QDs.[38] TEM together with energy-dispersive X-ray spectroscopy (EDS) was carried out. Fig. 2e shows that the EDS mapping images of Cs, Pb, Br, S, N, and C elements all overlap with the TEM image of $CsPbBr_3$-DPSI/MS composites, which indicates that $CsPbBr_3$ QDs with DPSI are uniformly distributed inside in the silica MS template. Fig. 2f gives the high-resolution TEM image of the

$CsPbBr_3$-DPSI/MS composite and the corresponding diffraction pattern, in which two lattice spacings of 0.33 nm and 0.29 nm are observed, corresponding to the (111) plane and (200) plane of cubic $CsPbBr_3$. The X-ray diffraction (XRD) result (Fig. 2g) also confirms the cubic $CsPbBr_3$ phase in the obtained $CsPbBr_3$-DPSI/MS composites.

Optical measurements were used to investigate the emission and the related electronic properties of the obtained $CsPbBr_3$-DPSI/MS composites. Compared with the reference sample ($CsPbBr_3$/MS composites), the PLQY of $CsPbBr_3$-DPSI/MS composites is significantly enhanced from 27.4% to 93.2% (Fig. 3a and b). This enhancement suggests a substantial reduction in non-radiative losses, which can be attributed to effective defect passivation. The PLQY of the obtained samples as a function of the DPSI additive amount in precursors is shown in Fig. S3 (ESI†). When increasing the DPSI additive amount from 15 to 44 mg, the PLQY of $CsPbBr_3$ nanocrystals gradually increases and reaches the highest PLQY at an DPSI additive amount of 37 mg. To get further insight into the recombination mechanism of the photogenerated carriers, we employed transient spectroscopies to investigate the PL decay process of the $CsPbBr_3$-DPSI/MS composites and the reference sample ($CsPbBr_3$/MS composites). As shown in Fig. 3c, the time-resolved photoluminescence (TRPL) decay curves are fitted using the biexponential equation

$$I_{(t)} = I_0 + a_1 \exp(-t/\tau_1) + a_2 \exp(-t/\tau_2) \qquad (1)$$

where a_1 and a_2 are amplitudes; τ_1 and τ_2 are lifetimes for fast and long PL decay processes (details shown in Table S1, ESI†).[39]
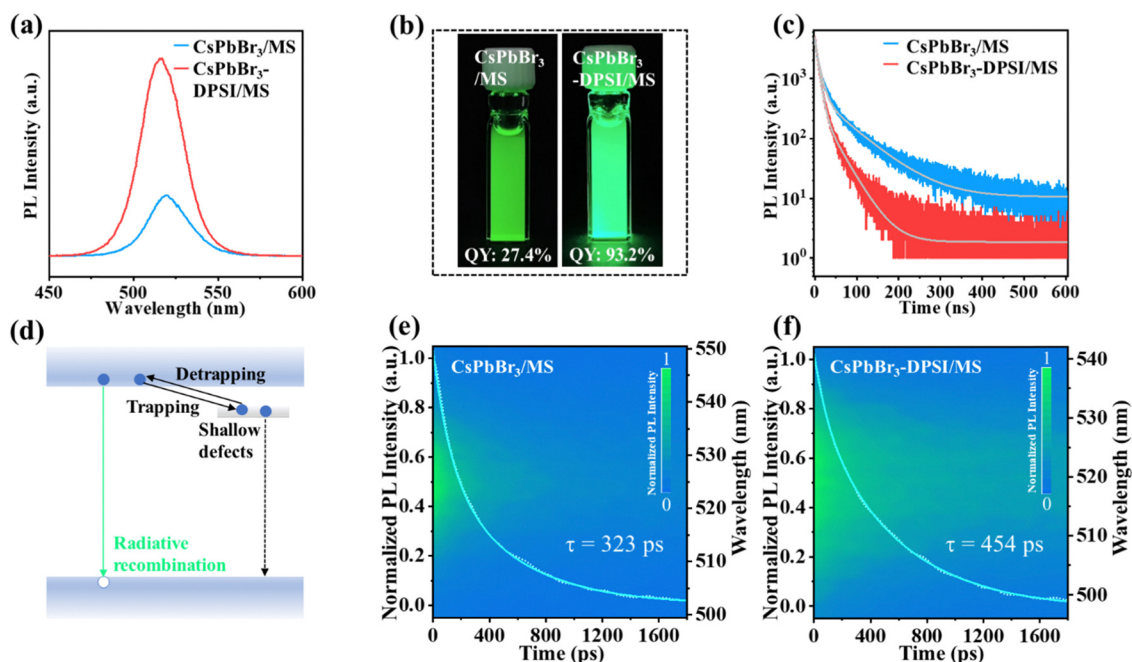

Fig. 3 Optical properties of $CsPbBr_3$ QDs. (a) PL spectra of the $CsPbBr_3$/MS and $CsPbBr_3$-DPSI/MS. (b) Photographs of the $CsPbBr_3$/MS and $CsPbBr_3$-DPSI/MS (immersed in water) under UV excitation at 365 nm. (c) TRPL decay curves of the $CsPbBr_3$/MS and $CsPbBr_3$-DPSI/MS. (d) Schematic representation of the PL processes related to the exciton and exciton–shallow defects interactions. Time- and wavelength-dependent PL mapping were measured with a streak camera under the illumination of a femtosecond laser of 405 nm (1 kHz, 200 fs) for (e) $CsPbBr_3$/MS and (f) $CsPbBr_3$-DPSI/MS.

3468 | *J. Mater. Chem. C*, 2024, **12**, 3465–3473

This journal is © The Royal Society of Chemistry 2024

For the CsPbBr$_3$-DPSI/MS composites, the fast and the long components are respectively 8.32 ns (78.91%) and 43.59 ns (21.09%), while those for the reference sample are respectively 11.97 ns (54.65%) and 96.88 ns (45.35%). The lifetime of the fast components agrees well with that of the exciton radiation recombination in CsPbBr$_3$.[40] According to the previous reports, apart from the nonradiative recombination, doped electrons can detrap from shallow defect states to conduction band minimum for radiative recombination with a longer lifetime than exciton radiation (see Fig. 3d).[39] Therefore, we attribute the long components to the interaction between excitons and defects. For CsPbBr$_3$-DPSI/MS composites, the significant percentage decrease for the long component is indicative of the defect passivation, and the percentage increase for the fast component indicates the improvement of the exciton radiation recombination. Furthermore, a streak camera equipped with a femtosecond laser of 405 nm (1 kHz, 200 fs) was used to get insights into the PL decay with the time scale of hundred picoseconds that is related to the surface state recombination (see Fig. 3e and f).[41] The average PL lifetime is extended from 323 ps for CsPbBr$_3$/MS composites to 454 ps for CsPbBr$_3$-DPSI/MS composites, which confirms the effective passivation on the surface of CsPbBr$_3$ QDs by DPSI. Besides, we have further compared the full width at half maxima (FWHM) of

CsPbBr$_3$-DPSI/MS composites with several reported phosphors (Table S2, ESI†). FWHM of CsPbBr$_3$-DPSI/MS can reach to 25 nm, which is comparable to that of previously reported CsPbBr$_3$-Beta composites and CsPbBr$_3$@glass nanocomposites.

Next, we investigated the stability of the CsPbBr$_3$-DPSI/MS composites against water, heat, and photoirradiation. The CsPbBr$_3$-DPSI/MS composites were stable in water for 250 hours with almost no drop in the PL intensity (Fig. S4, ESI†), indicating that the MS matrix provided excellent water resistance for inside CsPbBr$_3$ nanocrystals by isolating them from the external environment. As shown in Fig. 4a, when the heating temperature is increased from 300 K to 333 K and 373 K, the PL intensity of CsPbBr$_3$-DPSI/MS retains 84% and 41% of their initial PL intensity, respectively. In contrast, the PL intensity of CsPbBr$_3$/MS decreases to 65% and 25% of their initial intensity at 333 K and 373 K, respectively. These results indicate that the DPSI can enhance the heat stability of CsPbBr$_3$ QDs. In addition, DPSI can greatly improve the photo-stability of CsPbBr$_3$ QDs. Under blue light irradiation with a power density of 3500 W m^{-2}, the PL intensity of the CsPbBr$_3$-DPSI/MS composites is still maintained above 100% under irradiation for 48 h (Fig. 4b and d). In contrast, the PL intensity of the CsPbBr$_3$/MS composites drops to 41% of their initial values under the same irradiation for 38 h (Fig. 4c and d). These
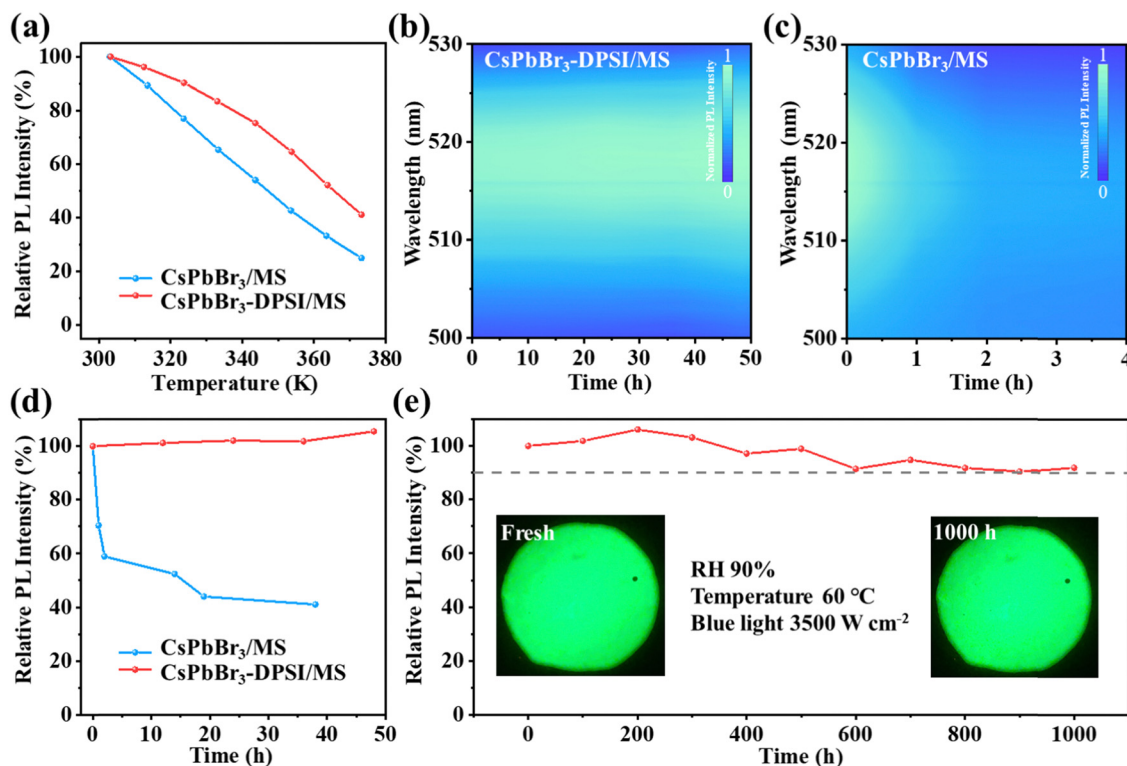

Fig. 4 Thermal and photo stability of the CsPbBr$_3$ QDs. (a) Temperature-dependent relative integrated PL intensity of the CsPbBr$_3$/MS and CsPbBr$_3$-DPSI/MS. Pseudo-color maps of the time-dependent PL spectra of the (b) CsPbBr$_3$-DPSI/MS and (c) CsPbBr$_3$/MS subjected to blue light irradiation. (d) Time-dependent relative integrated PL intensity of the CsPbBr$_3$/MS and CsPbBr$_3$-DPSI/MS subjected to blue light irradiation. (e) Time-dependent relative integrated PL intensity of the CsPbBr$_3$-DPSI/MS composites-based film subjected to the harsh aging conditions (temperature: 60 °C, relative humidity: 90%, blue light irradiation with a high power density of 3500 W m^{-2}), inset figures are photographs of the CsPbBr$_3$-DPSI/MS composite based film under 365 nm UV light irradiation.

This journal is © The Royal Society of Chemistry 2024

J. Mater. Chem. C, 2024, **12**, 3465–3473 | **3469**

results suggest that the improved photo and thermal stability of the CsPbBr$_3$-DPSI/MS composites originated from the effective passivation by DPSI, preventing the formation of photo- or thermal-induced defects in CsPbBr$_3$ QDs. Furthermore, to verify the overall stability of CsPbBr$_3$-DPSI/MS composites under the real application conditions of synergistic humidity, heat, and high-energy light irradiation, we conducted accelerated operational stability tests on these composites under high temperature (HT 60 °C), high humidity (RH 90%), and 3500 W m^{-2} blue light irradiation. After aging for 1000 h, the CsPbBr$_3$-DPSI/MS composites still retain 90% of their initial PL intensity (Fig. 4e). To the best of our knowledge, these CsPbBr$_3$-DPSI/MS composites represent the most stable CsPbBr$_3$ emitters in an accelerated aging test under synergistic humidity–heat–light conditions compared with the previously reported CsPbBr$_3$ emitters (Table S3, ESI†). Besides, these CsPbBr$_3$-DPSI/MS composites exhibit great chemical stability. We directly mixed these composites with 1 mol L^{-1} KI, 1 mol L^{-1} KCl, and 1 mol L^{-1} HCl aqueous solutions, respectively. The CsPbBr$_3$ nanocrystals maintain their own PL characteristics without obvious peak shifts or fluorescence quenching even after 72 hours (Fig. S5, ESI†).

The high luminescence efficiency and overall stability ensure that the CsPbBr$_3$-DPSI/MS composites are potentially applicable to commercial display and imaging applications, such as full-color LCD and X-ray scintillator materials.[42–44]

As a demo-of-concept, a diffusion plate based on the CsPbBr$_3$-DPSI/MS composites (CPB-plate) was fabricated by a hot-melt extrusion method, which was employed as down-converters for an LCD backlight (Fig. 5a). The PL spectrum of the CPB-plate exhibits a narrow green emission with the center peak at 520 nm (inset in Fig. 5a). Fig. 5b shows the construction of the LCD device equipped with a CPB-plate (CPB-LCD), where purple LED chips (composed of blue LED and K$_2$SiF$_6$:Mn^{4+} powders, Fig. S6, ESI†) were used to excite the emission of the CPB-plate and provide the red and blue light. Fig. S7 (ESI†) shows the transmittance spectrum of three primary colors in the LCD module. Fig. 5c gives the white-light spectra of the CPB-LCD and an ordinary commercial LCD (OC-LCD), respectively. In comparison, the green part of the spectrum in CPB-LCD is narrower than that in OC-LCD. Fig. 5d and e exhibit the spectra of three primary colors in CPB-LCD and OC-LCD, respectively. The three primary color coordinates of CPB-LCD and OC-LCD are shown in Table S4 (ESI†). Both the blue light and red light in CPB-LCD are similar to that in OC-LCD, while the FWHM of green light in CPB-LCD (19.3 nm) is smaller than that in OC-LCD (40.7 nm), which results in the color gamut area of CPB-LCD (111.7% NTSC) being wider than that of OC-LCD (95.2% NTSC) (Fig. 5f). The picture of a green gecko on the CPB-LCD presents a more vivid green color in comparison with the OC-LCD (Fig. 5g). These results prove that the
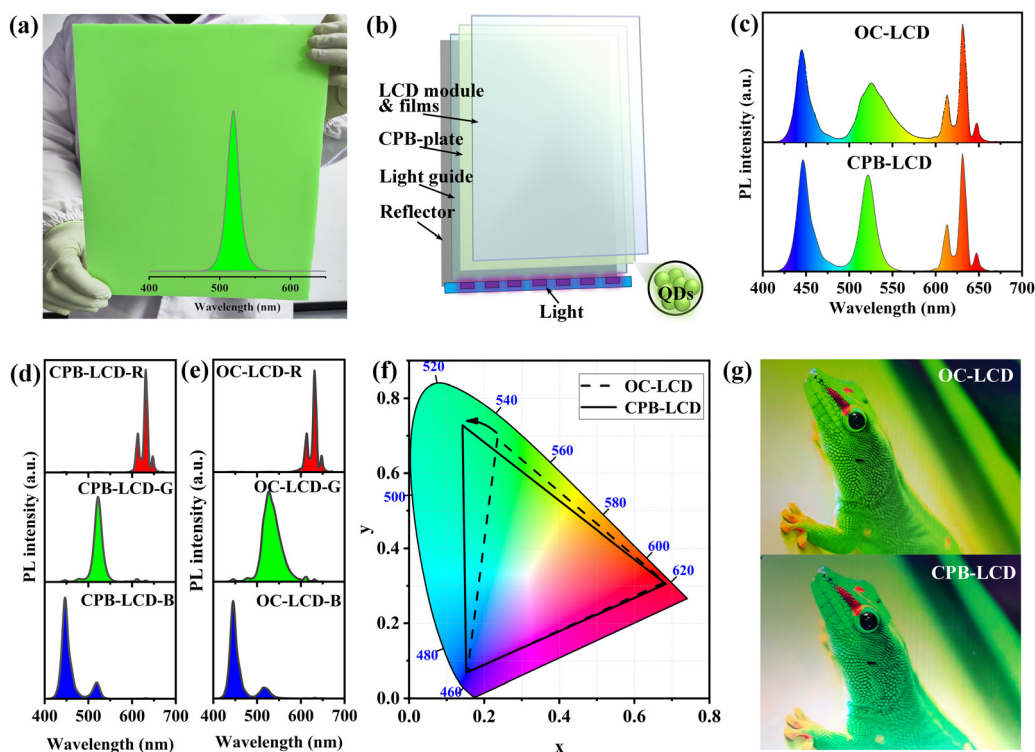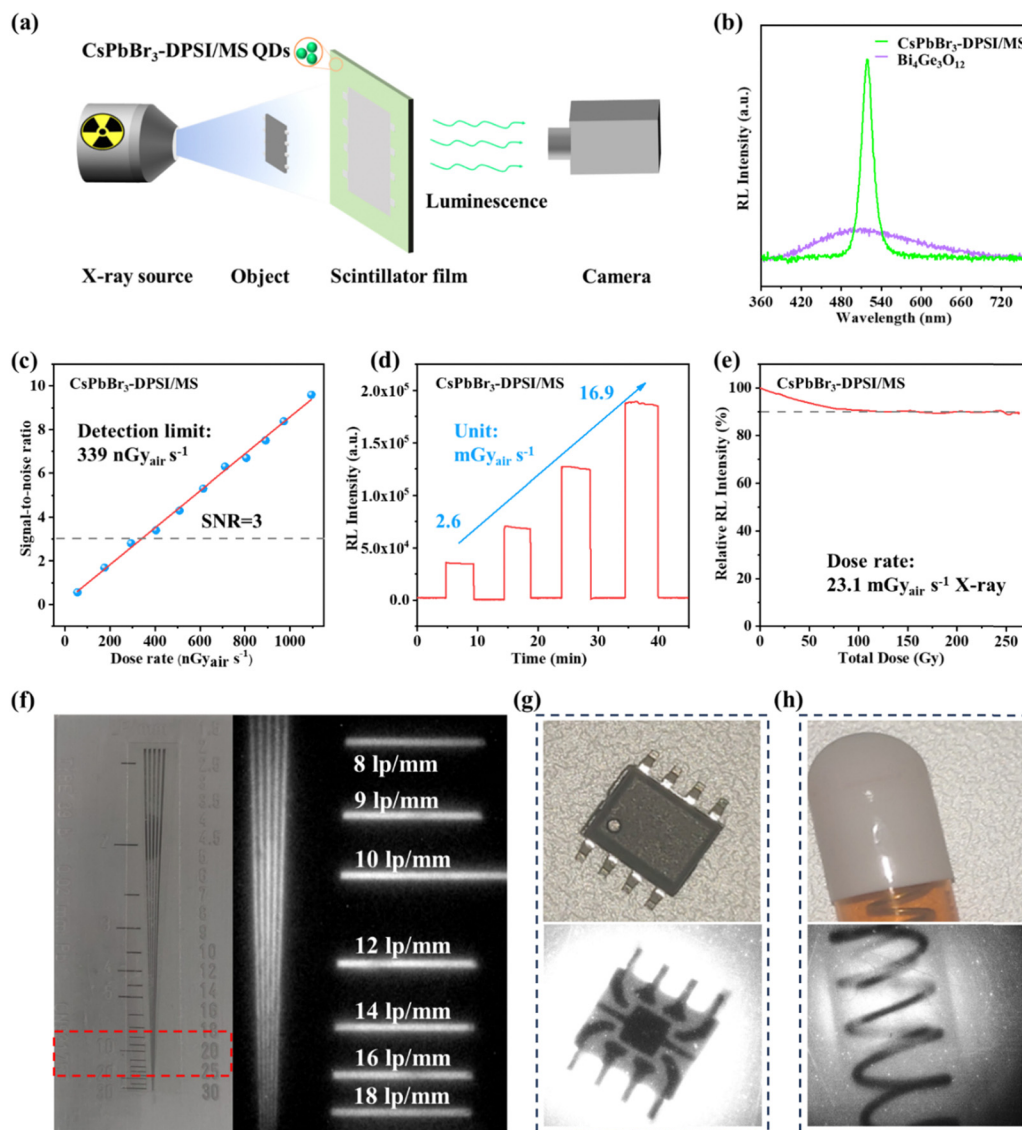

Fig. 5 Optical characterization and performance of LCD application based on CsPbBr$_3$-DPSI/MS composites. (a) Optical image and PL spectrum of the CPB-plate. (b) Schematic of the CPB-LCD construction. (c) White-light spectra of OC-LCD and CPB-LCD. (d) and (e) Spectra of three primary colors in CPB-LCD and OC-LCD, respectively. (f) Color gamut coverage of CPB-LCD and OC-LCD. (g) Pictures displayed on CPB-LCD and OC-LCD.

3470 | *J. Mater. Chem. C*, 2024, **12**, 3465–3473

This journal is © The Royal Society of Chemistry 2024

Fig. 6 Radioluminescence characterization of $CsPbBr_3$-DPSI/MS based scintillator film and X-ray imaging demonstrations. (a) Schematic of X-ray imaging system. (b) RL spectra of $CsPbBr_3$-DPSI/MS and $Bi_4Ge_3O_{12}$. (c) The signal-to-noise of X-ray response for the $CsPbBr_3$-DPSI/MS-based scintillator film as a function of X-ray dose rate. (d) RL intensity of the $CsPbBr_3$-DPSI/MS-based scintillator film under cyclical X-ray irradiation with a stepwise increased dose rate from 2.6 to 16.9 mGy_{air} s^{-1}. (e) Relative RL intensity of the $CsPbBr_3$-DPSI/MS-based scintillator film as a function of total X-ray dose under continuous irradiation of 23.1 mGy_{air} s^{-1} X-ray. (f) Bright-field (left) and X-ray (right) images of standard X-ray test pattern plate. (g) Bright-field (top) and X-ray (bottom) images of a chip. (h) Bright-field (top) and X-ray (bottom) images of a capsule containing an internal spring.

$CsPbBr_3$-DPSI/MS composites are a promising candidate for the fabrication of LCD with a wide color gamut.

Furthermore, the feasibility of the $CsPbBr_3$-DPSI/MS composites in an X-ray imaging detector was evaluated by a home-made X-ray imaging projection system, where an X-ray source, a test object, a $CsPbBr_3$-DPSI/MS composite film and a charge-coupled device (CCD) camera were placed in sequence as exhibited in Fig. 6a. Fig. S8 (ESI†) shows the calculated attenuation with coherent scattering of $CsPbBr_3$ at a different X-ray photon energy, indicating that the X-ray absorption efficiency of $CsPbBr_3$ is comparable to that of other commercial scintillators ($Bi_4Ge_3O_{12}$, CsI). Thanks to their strong X-ray absorption and high luminescence efficiency, the radioluminescence (RL)

intensity of $CsPbBr_3$-DPSI/MS composites is stronger than that of commercial $Bi_4Ge_3O_{12}$ scintillators (Fig. 6b). The X-ray imaging system based on the $CsPbBr_3$-DPSI/MS composites film exhibits a low detection limit of 339 nGy_{air} s^{-1} (Fig. 6c), which is about 16 times lower than that required for commercial computed tomography (5500 nGy_{air} s^{-1}).[45] Besides, the RL intensity of $CsPbBr_3$-DPSI/MS composites has a wide linear response range from 390 nGy_{air} s^{-1} to 23.1 mGy_{air} s^{-1}, which is beneficial for obtaining high-contrast images (Fig. S9, ESI†).[46] Impressively, the $CsPbBr_3$-DPSI/MS composites exhibit excellent radiation stability. As shown in Fig. 6d, under cyclical X-ray irradiation with a stepwise increase in the dose rate, the $CsPbBr_3$-DPSI/MS composites are extremely robust without

This journal is © The Royal Society of Chemistry 2024

J. Mater. Chem. C, 2024, **12**, 3465–3473 | **3471**

obvious degradation in the RL intensity. Then a fatigue test was performed on the CsPbBr$_3$-DPSI/MS composites with an accumulated irradiation dose of ≈ 262 Gy at room temperature (50 kV, dose rate ≈ 23.1 mGy$_{air}$ s^{-1}). As shown in Fig. 6e, even after exposure to such a high fluence and large dose of X-ray irradiation, the CsPbBr$_3$-DPSI/MS composites still retain 90% of their initial RL intensity, which is comparable to other perovskites or perovskite-like metal halide scintillators with outstanding stability, such as CsPbBr$_3$@PbBrOH (keep stable under the X-ray irradiation with a total dose of 0.338 Gy) and Cs$_3$Cu$_2$I$_5$ (following exposure to X-ray irradiation at a rate of 17.4 mGy$_{air}$ s^{-1} and a cumulative dose of 43 Gy, the RL intensity retains 78% of its initial value).[47,48] The X-ray imaging system based on the CsPbBr$_3$-DPSI/MS composite film achieves a spatial resolution of ≈ 16 lp mm^{-1}, as obtained from an X-ray image of a standard X-ray test pattern plate (Fig. 6f), which is even superior to most perovskite-based X-ray imaging systems (Table S5, ESI†). To assess the feasibility of the X-ray imaging system based on the CsPbBr$_3$-DPSI/MS composites, we presented several examples of non-destructive testing for objects with complex internal structures that are opaque to visible light. Fig. 6g and h show images of a chip and a capsule containing an internal spring under both white light and X-rays, respectively, where the internal structures of both samples can be clearly exhibited under X-ray irradiation. These experimental results highlight the great potential of the CsPbBr$_3$-DPSI/MS composites in high-resolution X-ray imaging.

4. Conclusions

In summary, CsPbBr$_3$-DPSI/MS composites with excellent PL properties and overall stability (against heat, moisture, and photo-irradiation) were synthesized through a solid-state synthesis method. In these composites, CsPbBr$_3$ QDs were passivated by DPSI and followed by further encapsulation by silica MS matrices, leading to an enhanced PLQY of 93.2% and remarkable stability under harsh synergistic humidity–heat–light aging conditions. The CsPbBr$_3$-DPSI/MS composites retained more than 90% of their initial PL intensity after aging for 1000 hours under the following synergistic conditions: temperature of 60 °C, relative humidity of 90%, and blue light irradiation with a power density of 3500 W m^{-2}. The LCD backlight module utilizing these stable composites shows a wide color gamut of 111.7% NTSC. Besides, these CsPbBr$_3$-DPSI/MS composites were applied in X-ray imaging with excellent radiation stability, a low detection limit of 339 nGy$_{air}$ s^{-1}, and a spatial resolution of 16 lp mm^{-1}. Our work clarifies the crucial roles of defect passivation and encapsulation in achieving highly efficient and stable CsPbBr$_3$ QDs, and promising practical application of perovskite emitters.

Author contributions

Peng Wang (data curation: equal; formal analysis: equal; writing – original draft: equal), Zhaoyu Wang (formal analysis: equal; methodology: equal; writing – original draft: equal; writing – review & editing: equal), Meiyi Zhu (data curation: equal; methodology: equal; writing – review & editing: equal), QiuTing Cai (methodology: supporting), Hanyan Huang (conceptualization: supporting), Chengyuan Tang (formal analysis: supporting), Haoran Zhang (methodology: supporting), Chao Fan (conceptualization: lead; formal analysis: lead; methodology: lead; writing – original draft: lead), Xingliang Dai (conceptualization: equal; data curation: equal), Haiping He (conceptualization: equal; validation: lead; writing – review & editing: equal), Zhizhen Ye (funding acquisition: lead; project administration: equal; writing – review & editing: lead).

Conflicts of interest

There are no conflicts to declare.

Acknowledgements

References

1 Y. Li, X. Zhang, H. Huang, S. V. Kershaw and A. L. Rogach, *Mater. Today*, 2020, **32**, 204–221.

2 S. Liang, M. Zhang, G. M. Biesold, W. Choi, Y. He, Z. Li, D. Shen and Z. Lin, *Adv. Mater.*, 2021, **33**, 2005888.

3 Y. Wei, Z. Cheng and J. Lin, *Chem. Soc. Rev.*, 2019, **48**, 310–350.

4 Q. Zhong, M. Cao, Y. Xu, P. Li, Y. Zhang, H. Hu, D. Yang, Y. Xu, L. Wang, Y. Li, X. Zhang and Q. Zhang, *Nano Lett.*, 2019, **19**, 4151–4157.

5 M. Zhao, Q. Zhang and Z. Xia, *Mater. Today*, 2020, **40**, 246–265.

6 H. Li, Y. Gao, X. Ying, Y. Feng, M. Zhu, D. Zhang, G. Lu, R. Tao, Q. Cai, H. He, X. Dai, Z. Ye and J. Huang, *Chem. Eng. J.*, 2023, **454**, 140038.

7 X. K. Liu, W. Xu, S. Bai, Y. Jin, J. Wang, R. H. Friend and F. Gao, *Nat. Mater.*, 2021, **20**, 10–21.

8 Y. F. Lan, J. S. Yao, J. N. Yang, Y. H. Song, X. C. Ru, Q. Zhang, L. Z. Feng, T. Chen, K. H. Song and H. B. Yao, *Nano Lett.*, 2021, **21**, 8756–8763.

3472 | *J. Mater. Chem. C*, 2024, **12**, 3465–3473

This journal is © The Royal Society of Chemistry 2024

9 J. Yuan, A. Hazarika, Q. Zhao, X. Ling, T. Moot, W. Ma and J. M. Luther, *Joule*, 2020, **4**, 1160–1185.

10 X. Zhang, H. Huang, X. Ling, J. Sun, X. Jiang, Y. Wang, D. Xue, L. Huang, L. Chi, J. Yuan and W. Ma, *Adv. Mater.*, 2022, **34**, 2105977.

11 J. H. Heo, D. H. Shin, J. K. Park, D. H. Kim, S. J. Lee and S. H. Im, *Adv. Mater.*, 2018, **30**, 1801743.

12 S. Cho, S. Kim, J. Kim, Y. Jo, I. Ryu, S. Hong, J. J. Lee, S. Cha, E. B. Nam, S. U. Lee, S. K. Noh, H. Kim, J. Kwak and H. Im, *Light: Sci. Appl.*, 2020, **9**, 156.

13 M. N. An, S. Park, R. Brescia, M. Lutfullin, L. Sinatra, O. M. Bakr, L. De Trizio and L. Manna, *ACS Energy Lett.*, 2021, **6**, 900–907.

14 L. Chen, M. He, W. Gong, P. Hu, S. Yuan, A. Chen, L. Wei, Q. Zhang and Q. Li, *Nano Energy*, 2023, **108**, 108235.

15 S. Zhang, Z. Liu, W. Zhang, Z. Jiang, W. Chen, R. Chen, Y. Huang, Z. Yang, Y. Zhang, L. Han and W. Chen, *Adv. Energy Mater.*, 2020, **10**, 2001610.

16 J. I. Kim, Q. Zeng, S. Park, H. Lee, J. Park, T. Kim and T. W. Lee, *Adv. Mater.*, 2023, 2209784.

17 X. Wang, Z. Bao, Y.-C. Chang and R.-S. Liu, *ACS Energy Lett.*, 2020, **5**, 3374–3396.

18 W. J. Mir, A. Alamoudi, J. Yin, K. E. Yorov, P. Maity, R. Naphade, B. Shao, J. Wang, M. N. Lintangpradipto, S. Nematulloev, A. H. Emwas, A. Genovese, O. F. Mohammed and O. M. Bakr, *J. Am. Chem. Soc.*, 2022, **144**, 13302–13310.

19 D. N. Dirin, B. M. Benin, S. Yakunin, F. Krumeich, G. Raino, R. Frison and M. V. Kovalenko, *ACS Nano*, 2019, **13**, 11642–11652.

20 K. Xing, S. Cao, X. Yuan, R. Zeng, H. Li, B. Zou and J. Zhao, *Phys. Chem. Chem. Phys.*, 2021, **23**, 17113–17128.

21 A. Loiudice, S. Saris, E. Oveisi, D. T. L. Alexander and R. Buonsanti, *Angew. Chem., Int. Ed.*, 2017, **56**, 10696–10701.

22 Q. Zhang, B. Wang, W. Zheng, L. Kong, Q. Wan, C. Zhang, Z. Li, X. Cao, M. Liu and L. Li, *Nat. Commun.*, 2020, **11**, 31.

23 H. Dong, S. Tian, X. Sun, I. S. Mukhin, R. M. Islamova, G. Li and J. Tian, *Adv. Opt. Mater.*, 2023, **11**, 2300309.

24 S. Tian, X. Zhou, C. Bi, X. Sun, M. Zhang, S. Yang and J. Tian, *Adv. Opt. Mater.*, 2022, **10**, 2200751.

25 B. Li, Y. Zhang, Y. Xu and Z. Xia, *J. Mater. Chem. C*, 2021, **9**, 12118–12123.

26 S. X. Li, Y. Pan, W. M. Wang and Y. Li, *Chem. Eng. J.*, 2022, **434**, 134593.

27 S. Liao, Z. Yang, J. Lin, S. Wang, J. Zhu, S. Chen, F. Huang, Y. Zheng and D. Chen, *Adv. Funct. Mater.*, 2023, **33**, 2210558.

28 S. Chen, J. Lin, J. Huang, T. Pang, Q. Ye, Y. Zheng, X. Li, Y. Yu, B. Zhuang and D. Chen, *Adv. Funct. Mater.*, 2024, **34**, 2309293.

29 S. Chen, J. Lin, S. Zheng, Y. Zheng and D. Chen, *Adv. Funct. Mater.*, 2023, **33**, 2213442.

30 J. Lin, Y. Lu, X. Li, F. Huang, C. Yang, M. Liu, N. Jiang and D. Chen, *ACS Energy Lett.*, 2021, **6**, 519–528.

31 Y. Zhang, L. Han, B. Li and Y. Xu, *Chem. Eng. J.*, 2022, **437**, 135290.

32 C. Fan, H. Liu, J. Zhou, X. Dai, H. He and Z. Ye, *InfoMat*, 2023, **5**, 12417.

33 M. R. Kar, S. Ray, B. K. Patra and S. Bhaumik, *Mater. Today Chem.*, 2021, **20**, 100424.

34 J. Li, D. Zhou, Y. Liu, Y. Chen, J. Chen, Y. Yang, Y. Gao and J. Qiu, *ACS Appl. Mater. Interfaces*, 2023, **15**, 22219–22230.

35 T. Xuan, S. Guo, W. Bai, T. Zhou, L. Wang and R.-J. Xie, *Nano Energy*, 2022, **95**, 107003.

36 S. Liu, Z. Guo, X. Wu, X. Liu, Z. Huang, L. Li, J. Zhang, H. Zhou, L. D. Sun and C. H. Yan, *Adv. Mater.*, 2023, **35**, 2208078.

37 B. Guo, R. Lai, S. Jiang, L. Zhou, Z. Ren, Y. Lian, P. Li, X. Cao, S. Xing, Y. Wang, W. Li, C. Zou, M. Chen, Z. Hong, C. Li, B. Zhao and D. Di, *Nat. Photonics*, 2022, **16**, 637–643.

38 J. Zhang, X. Xing, D. Qian, A. Wang, L. Gu, Z. Kuang, J. Wang, H. Zhang, K. Wen, W. Xu, M. Niu, X. Du, L. Yuan, C. Cao, Y. Cao, L. Zhu, N. Wang, C. Yi, W. Huang and J. Wang, *Adv. Funct. Mater.*, 2022, **32**, 2111578.

39 Y. Huang, F. Li, L. Qiu, F. Lin, Z. Lai, S. Wang, L. Lin, Y. Zhu, Y. Wang, Y. Jiang and X. Chen, *ACS Appl. Mater. Interfaces*, 2019, **11**, 26384–26391.

40 G. H. Ahmed, J. Yin, O. M. Bakr and O. F. Mohammed, *ACS Energy Lett.*, 2021, **6**, 1340–1357.

41 S. W. Eaton, M. Lai, N. A. Gibson, A. B. Wong, L. Dou, J. Ma, L. W. Wang, S. R. Leone and P. Yang, *Proc. Natl. Acad. Sci. U. S. A.*, 2016, **113**, 1993–1998.

42 F. Cao, D. Yu, W. Ma, X. Xu, B. Cai, Y. M. Yang, S. Liu, L. He, Y. Ke, S. Lan, K. L. Choy and H. Zeng, *ACS Nano*, 2020, **14**, 5183–5193.

43 A. Jana, S. Cho, S. A. Patil, A. Meena, Y. Jo, V. G. Sree, Y. Park, H. Kim, H. Im and R. A. Taylor, *Mater. Today*, 2022, **55**, 110–136.

44 F. Zhou, Z. Li, W. Lan, Q. Wang, L. Ding and Z. Jin, *Small Methods*, 2020, **4**, 2000506.

45 H. Wei, Y. Fang, P. Mulligan, W. Chuirazzi, H.-H. Fang, C. Wang, B. R. Ecker, Y. Gao, M. A. Loi, L. Cao and J. Huang, *Nat. Photonics*, 2016, **10**, 333–339.

46 W. Ma, T. Jiang, Z. Yang, H. Zhang, Y. Su, Z. Chen, X. Chen, Y. Ma, W. Zhu, X. Yu, H. Zhu, J. Qiu, X. Liu, X. Xu and Y. M. Yang, *Adv. Sci.*, 2021, **8**, 2003728.

47 H. Guo, Y. Zhu, Q. Zhao, Q. Jiang, Y. Ma, J. Chen, L. Song, Z. Shi and C. Xu, *Sci. China Mater.*, 2023, **66**, 2004–2012.

48 Z. Wang, Y. Wei, C. Liu, Y. Liu and M. Hong, *Laser Photonics Rev.*, 2023, **17**, 2200851.

This journal is © The Royal Society of Chemistry 2024

J. Mater. Chem. C, 2024, **12**, 3465–3473 | **3473**